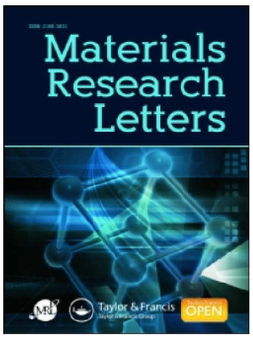

Materials Research Letters

ISSN: (Print) 2166-3831 (Online) Journal homepage: https://www.tandfonline.com/loi/tmrl20

Dislocation plasticity in FeCoCrMnNi high-entropy alloy: quantitative insights from *in situ* transmission electron microscopy deformation

Subin Lee, María Jazmin Duarte, Michael Feuerbacher, Rafael Soler, Christoph Kirchlechner, Christian H. Liebscher, Sang Ho Oh & Gerhard Dehm

To cite this article: Subin Lee, María Jazmin Duarte, Michael Feuerbacher, Rafael Soler, Christoph Kirchlechner, Christian H. Liebscher, Sang Ho Oh & Gerhard Dehm (2020) Dislocation plasticity in FeCoCrMnNi high-entropy alloy: quantitative insights from *in situ* transmission electron microscopy deformation, Materials Research Letters, 8:6, 216-224, DOI: 10.1080/21663831.2020.1741469

To link to this article: https://doi.org/10.1080/21663831.2020.1741469

MATER. RES. LETT.
2020, VOL. 8, NO. 6, 216–224
https://doi.org/10.1080/21663831.2020.1741469

MATERIALS RESEARCH LETTERS
Taylor & Francis
Taylor & Francis Group

ORIGINAL REPORT

Dislocation plasticity in FeCoCrMnNi high-entropy alloy: quantitative insights from *in situ* transmission electron microscopy deformation

Subin Lee [a,b], María Jazmin Duarte [a], Michael Feuerbacher [c], Rafael Soler[a], Christoph Kirchlechner [a], Christian H. Liebscher[a], Sang Ho Oh [d] and Gerhard Dehm[a]

[a]Structure and Nano-/ Micromechanics of Materials, Max-Planck-Institut für Eisenforschung, Düsseldorf, Germany; [b]Center for Integrated Nanostructure Physics, Institute for Basic Science (IBS), Suwon, Republic of Korea; [c]Ernst Ruska-Centre for Microscopy and Spectroscopy with Electrons and Peter Grünberg Institute, Forschungszentrum Jülich GmbH, Jülich, Germany; [d]Department of Energy Science, Sungkyunkwan University (SKKU), Suwon, Republic of Korea

ABSTRACT

The mechanical properties of high-entropy alloys (HEAs) are still not deeply understood. Detailed knowledge of the strengthening mechanism, especially, the atomistic origin of solid solution hardening and its interplay with dislocation plasticity is needed. Here, we report on the dislocation glide behavior of a FeCoCrNiMn face-centered cubic (FCC) single crystal studied by *in situ* deformation in a transmission electron microscope (TEM). The threshold shear stress for dislocation glide in a thin foil is measured from dislocation curvature as exceeding 400 MPa. Interestingly, dislocations are prevented from straightening upon unloading due to high frictional stresses.

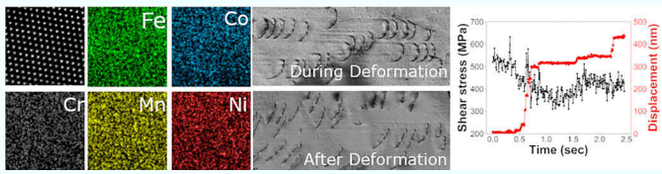

IMPACT STATEMENT

The fiction stress for dislocation glide in a FeCoCrMnNi HEA is assessed by direct measurement of dislocation line curvature during *in situ* TEM deformation, which is higher compared to other FCC metals, explaining the outstanding yield and flow stress of the HEA.

ARTICLE HISTORY
Received 4 December 2019

KEYWORDS
High-entropy alloys; dislocation plasticity; *in situ* TEM; strengthening mechanisms; lattice friction stress

1. Introduction

HEAs have been intensively investigated not only due to fundamental scientific interest but also their outstanding mechanical properties, especially high ductility and fracture toughness at cryogenic temperature [1–3]. Among hundreds of different combinations of principal elements, the equiatomic FeCoCrMnNi alloy, the so-called 'Cantor alloy' [4,5], has been studied as a model HEAs system. Dislocation slip by dissociated dislocations is the dominant deformation process of Cantor alloy at room temperature, while deformation twinning is a key strengthening mechanism at cryogenic temperature [6].

The initial assumption was that the core effects of HEAs, such as their high entropy effect or severe lattice distortion, have a strong influence on strengthening mechanisms [2,5]. Recent investigations indicate that the lattice of a highly concentrated solid solution of constituent elements with differing atomic radii experiences severe distortions contributing to the strength of the alloy [7,8]. The lattice friction stress—which is the shear stress required for dislocations to glide—is expected to be higher than that of classical alloys and is accepted as a key strengthening mechanism [7]. Also, the local variation of the physical properties was observed, for instance, the stacking fault width of Cantor alloy shows a large spatial variation observed by high-resolution scanning TEM (STEM) [9] and Monte Carlo simulation [10]. It can be local elemental fluctuations in the statistical occupation probabilities of atomic sites, or short-range order (SRO)

CONTACT Sang Ho Oh sanghooh@skku.edu; Gerhard Dehm dehm@mpie.de

Supplemental data for this article can be accessed here. https://doi.org/10.1080/21663831.2020.1741469

which has been suggested by experimental [11,12] and theoretical [13] studies.

Mechanism of dislocation plasticity, the way they nucleate, multiply and interact with other defect structures, is the key to understand the mechanical properties of HEAs and is therefore of fundamental interest. However, to date, only a few studies reported on the mechanisms of dislocation-based plasticity in HEAs [14,15]. The fundamental understanding of the underlying deformation and strengthening mechanism at the micro- and nano-scale remain elusive and the nano-scale structural characteristics of HEAs, which can directly affect the dislocation glide motion, have also not been understood comprehensively.

The main objective of this study is to deepen the understanding of strengthening mechanisms in the FCC FeCoCrMnNi alloy using *in situ* TEM mechanical testing. The local composition and microstructure characterized by (S)TEM and atom probe tomography (APT) are correlated with the stress–strain curves and dislocation motion measured by *in situ* TEM deformation tests. Based on the quantitative analysis of dislocation glide motion, we examine the threshold stress for dislocation glide and relate the observations to strengthening mechanisms of the alloy.

2. Materials and methods

2.1. Sample preparation

A single crystal FeCoCrMnNi HEA was prepared by the Czochralski method from an equiatomic melt of high-purity elements. The composition of the alloy measured by STEM energy dispersive X-ray spectroscopy (EDS) and APT is summarized in Table 1. The Mn content is lower than that of the other constituent elements and Fe and Co exceed from the equiatomic composition. The errors in the composition represent the standard deviation of 10 different EDS measurements and different APT samples.

TEM samples for dislocation structure analysis were prepared by using the ion slicer (EM-09100IS, JEOL). For atomic-scale EDS analysis, samples were prepared by a focused ion beam (FIB) lift-out method which utilizes a 30 and 5 kV Ga ion beam (JIB-4601F, JEOL). Tensile straining samples were prepared by the site-specific FIB lift-out method and glued on a custom made Cu straining grid (orange-colored part in Figure 4(a)) by Pt deposition in a FIB. TEM samples were further milled by low energy Ar milling at 1, 0.5, and 0.3 kV for 5 min at each step to minimize the FIB-induced damage (NanoMill, Fischione). Submicron pillars were fabricated by FIB annular milling at 30 kV (Auriga®, Zeiss).

2.2. Transmission electron microscopy

An aberration-corrected TEM operated at 300 kV (JEM-ARM300CF, JEOL) was used for conventional TEM microstructure analysis at bright- and dark-field imaging modes and for chemical analysis by EDS at STEM mode. *In situ* tensile straining tests were carried out by using a straining holder (Model 654, Gatan). *In situ* TEM compression tests on the submicron pillars were performed by using a TEM operated at 200 kV (JEM-2200FS, JEOL) equipped with a nanoindentation holder (PI-95, Hysitron).

2.3. Atom probe tomography

The needle samples for APT were prepared by FIB lift-out and tip milling (Helios 600i, FEI). A final milling step using 5 kV and 23 pA was conducted to minimize Ga implantation. APT measurements were conducted in 5 different samples yielding similar results (LEAP 5000 XS, Cameca). The measurements were set at temperatures of 50 or 60 K in voltage mode at 250 kHz with a 15% pulse fraction for evaporation. APT data were reconstructed using the software IVAS 3.8.2.

3. Results and discussion

3.1. Dislocation structure

A representative dislocation structure before deformation recorded by weak-beam dark-field imaging is shown in Figure 1(a). A noticeable feature is the dislocation array with more than 30 evenly-spaced dislocations lying on the same slip plane (Figure 1(b)), indicating the planar slip dominant deformation. The dislocation density was estimated to be on the order of $10^{13}\ m^{-2}$ (in specific, $1.1 \pm 0.4 \times 10^{13}\ m^{-2}$ by line intersection method and $5.3 \pm 0.7 \times 10^{13}\ m^{-2}$ by aerial density measurement using image processing). Due to the predominance of local planar slips the dislocation density is inhomogeneous in submicrometer length scales.

Table 1. Chemical composition of the alloy measured by STEM-EDS and APT.

	Elements (at.%)				
	Fe	Co	Cr	Mn	Ni
STEM-EDS	24.2 ± 0.1	24.1 ± 0.2	19.8 ± 0.3	12.2 ± 0.3	19.7 ± 0.3
APT	24.21 ± 0.15	22.48 ± 0.11	21.68 ± 0.15	12.40 ± 0.11	19.23 ± 0.11

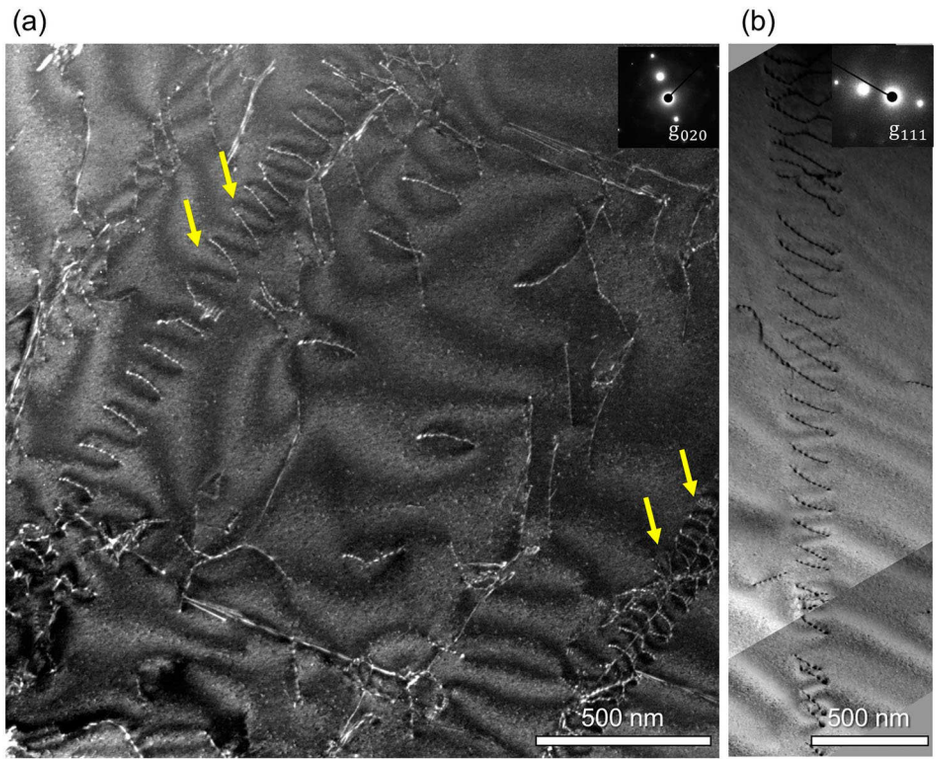

Figure 1. Dislocation structure before deformation. (a) Weak-beam dark-field TEM micrograph showing a high density of dislocations in arrays (yellow arrows). (b) Weak-beam dark-field TEM image showing dislocation arrays of planar slip. The insets show the diffraction condition.

3.2. Chemical analysis

To assess the local composition, we conducted elemental mapping using STEM-EDS (Figure 2(a,b)). Both, low magnification maps and also atomic-scale elemental maps show the random distribution of five elements without any sign of an ordered structure, clusters or precipitates. The electron diffraction also shows clear FCC single crystal patterns without superlattice reflections indicating a possible ordering or an intermetallic phase (Figure 1). And the sharp intensity maximum and the round shape of the reflections in the diffraction patterns indicate a single phase FCC crystal.

The APT investigation indicates a homogeneous chemical distribution of all constituting elements (Figure 2(c)). The concentration maps show only small composition fluctuations around the mean element content and no indication of chemical partitioning. Cluster analysis does not show evidence of precipitates or nanoscale clusters. Distribution analyses using different box sizes (50–200 ions) show that the experimental probability distribution closely follows a binomial distribution, indicating a random dispersion of all constituting elements (Figure 2(d)). The Pearson coefficient, of all elements is measured to be close to zero (e.g. for a 150 ions box size, $\mu_{Fe} = 0.0569$, $\mu_{Co} = 0.0643$, $\mu_{Cr} = 0.0595$, $\mu_{Mn} = 0.0687$, $\mu_{Ni} = 0.0711$), further suggesting a random distribution [16]. The nearest neighbor (NN) distributions for the 1st, 5th and 10th neighbors in Figure 2(e–i) show also a negligible difference with respect to a random distribution. The analyses of the higher order NN distributions are more sensitive to detect clustering, which is not observed in the current data.

However, before drawing conclusions on the absence of local clusters or ordered structures, the resolution and detection limit of both experimental approaches have to be considered. The lateral resolution of STEM-EDS in an aberration-corrected microscope is comparable to the electron probe size, which is less than 200 pm [17]. The depth resolution of the STEM-EDS, however, may not be sufficient enough to resolve potential SRO if existing, as the EDS signal is generated from the entire atomic column due to strong electron channeling effects. The formation of surface oxide in metallic materials is also a challenge. The detection limit of elemental species by APT is in the lower ppm range, but its spatial resolution is limited by anomalies in the field evaporation process and the detection efficiency. Local fluctuation in the evaporation rate should be more pronounced in multi-element composites like HEAs because of the strongly

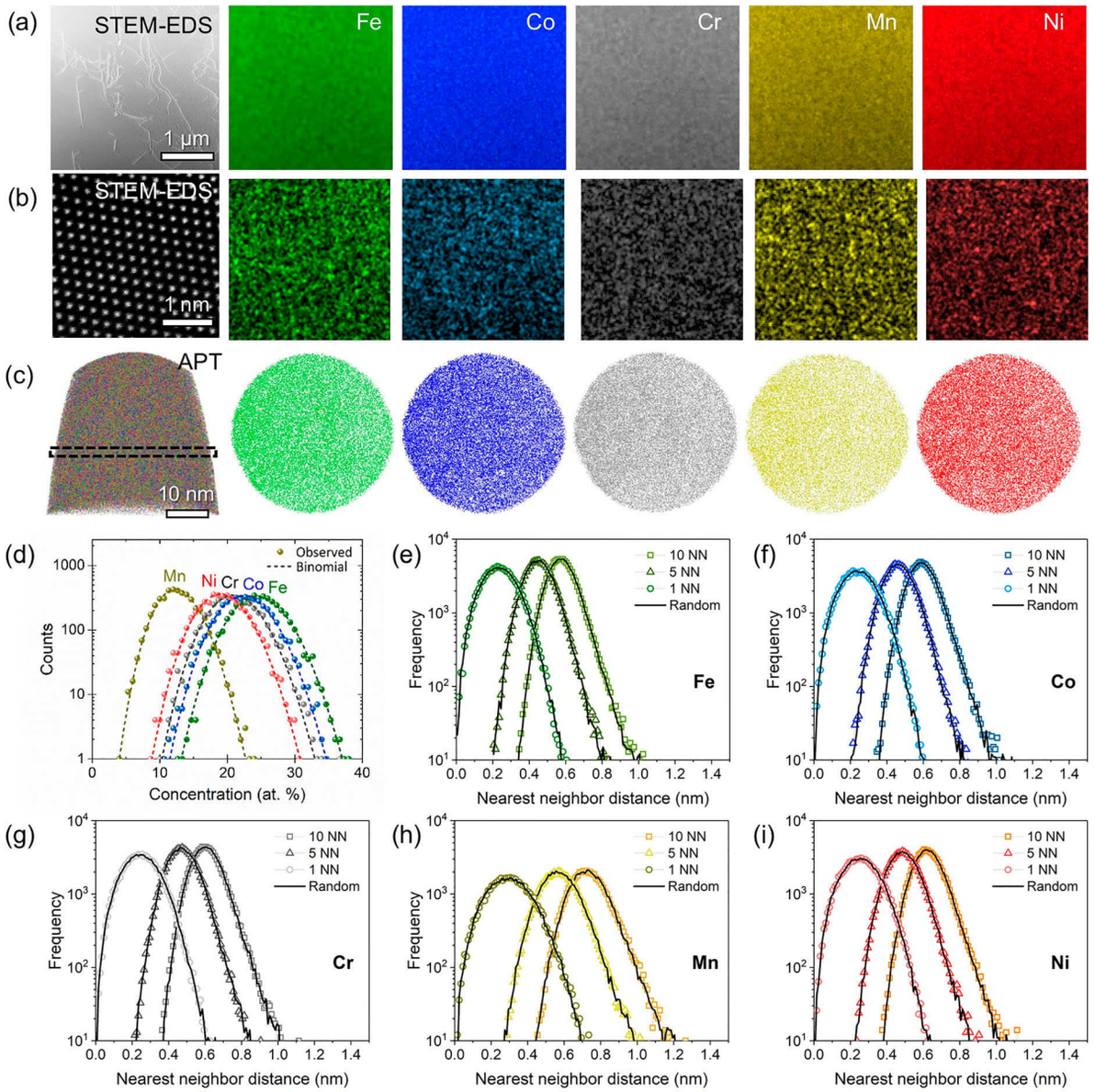

Figure 2. Chemical analysis by STEM-EDS and APT. (a) Low-magnification and (b) atomic-scale STEM-EDS elemental maps. (c) APT elemental distribution in a 3 nm slice corresponding to the black dotted region in the overview image. (d) Frequency distribution analysis (150 ions box size) and statistical comparison with a random distribution. (e–i) The nearest neighbor distribution for the 1st, 5th and 10th neighbor of each constituting element.

fluctuating nearest neighbor elements, which leads to differences in the interatomic bond strength. Additional aberrations in ion trajectories can be introduced at interfaces of nanoscale clusters. Finally, the dimensions of the reconstructed specimen must be considered as it limits the observations to small volumes of a few hundreds of nm in depth. In summary, no evidence of subnanometer-sized clusters or SRO was detected in the investigated HEA within the spatial resolution of STEM-EDS and APT, which is around 1 nm.

3.3. *Mechanical size effects in submicron pillars*

The mechanical properties of this alloy were investigated by micromechanical testing. Three pillars having a middle diameter of 280 nm (Pillar 1–3) and a pillar with 140 nm in diameter (Pillar 4) were tested, the corresponding SEM and TEM images after deformation are shown in Figure 3(a,b). Under [513] loading condition, $(1\bar{1}1)[110]$ slip was primarily activated (red arrows), followed by slip activities of the $(111)[\bar{1}10]$ slip

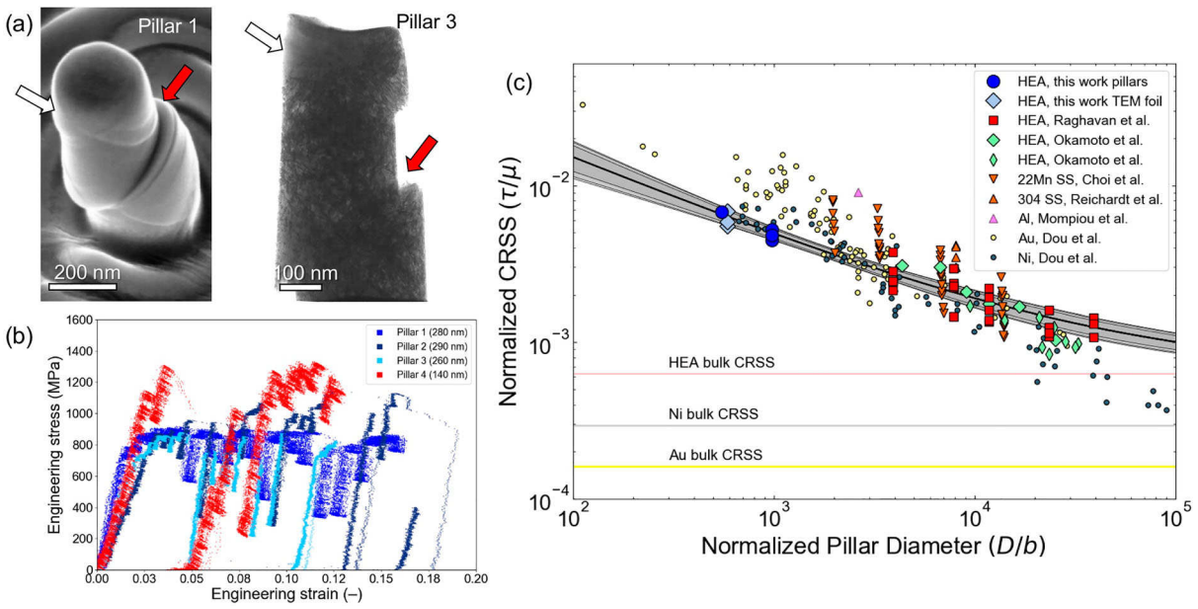

Figure 3. Microcompression of submicron pillars in TEM. (a) SEM and STEM micrographs after compression. Red and white arrows represent the primary and secondary slip planes, respectively. (b) Engineering stress-strain curve of each pillar. (c) Size dependence of the shear stress at 1% engineering strain measured from micropillars. Shear stress from submicron pillars deformed in TEM is plotted together with previously published results of *in situ* SEM testing with the same bulk material (red squares) [18] and other FCC materials data [19,20,23–25].

system (white arrows) with Schmid factors of 0.49 and 0.42, respectively. Detailed dislocation plasticity was difficult to be analyzed by STEM images because of (1) surface defects induced by FIB milling and (2) the high dislocation density. Deformation-induced twinning was observed neither in diffraction patterns nor in bright-filed images even after 20% strain.

To examine mechanical size effects in these pillars, the engineering stress at 1% plastic strain of each pillar was used to calculate the critical resolved shear stress (CRSS), $\tau_{1\%}$, which was then plotted over the pillar diameter (Figure 3(c)). Also, Figure 3(c) includes the corresponding data of micron-sized compression pillars made of the identical bulk single crystal [18]. For comparison with other FCC metals, the pillar diameter and CRSS are normalized by the Burgers vector and the shear modulus, respectively [19]. Then, the data were fitted with the size power-law relationship [19]

$$\frac{\tau_{1\%}}{\mu} = k\left(\frac{D}{b}\right)^{-m} + \frac{\tau_{\text{bulk}}}{\mu}, \tag{1}$$

where D is the pillar diameter, μ is the shear modulus, b is the magnitude of the Burgers vector and k is a fitting parameter. Solid lines represent 90%, 95% and 99% confidence intervals of the equation. To determine the size scaling exponent, m, we have further measured the bulk shear stress τ_{bulk} using macro compression testing, which was 50.4 ± 2.0 MPa. The size exponent was calculated as 0.53 ± 0.03 which is slightly smaller compared to other FCC metals, for instance, 0.70 for austenitic steel [20], 0.64 for Ni [21], 0.61 and 1.07 for Au [22]. However, these literature values are even underestimated because the authors did not include the bulk shear strength. Mechanical data of other Cantor alloy micropillar [23] shows a slightly lower stress level and a steeper slope in the size scaling plot, which might originate from different initial dislocation densities and heat treatments.

The smaller size scaling exponent in our results indicates that its strength is less sensitive to the size change than other FCC metals. The dislocation density, one possibility for the small size exponent, was not high enough to dominate strengthening by Taylor hardening. Therefore, the smaller size scaling exponent of HEAs suggests that other inherent strengthening mechanisms, such as solid solution hardening or a high lattice friction stress, are dominant.

3.4. Direct observation of dislocation plasticity

Detailed dislocation plasticity was analyzed by uniaxial *in situ* TEM tensile tests (Figure 4 and Supplementary Video 1,2). At the initial deformation, the Pt protection layer was cracked first as shown in Figure 4(c) which is the STEM image after the deformation. As the strain becomes localized at the crack tip, avalanche-like dislocation nucleation and multiplication occurred in the HEA

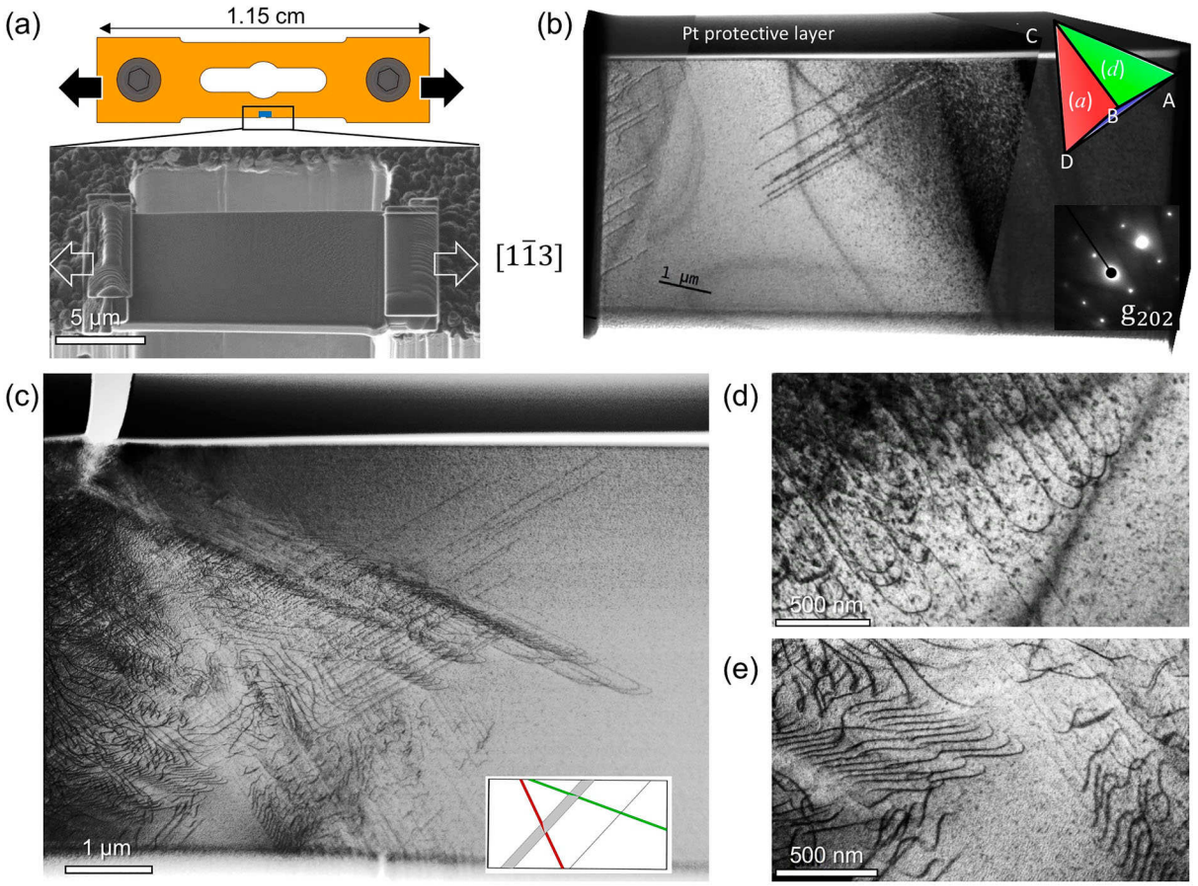

Figure 4. Dislocation structure before and after *in situ* TEM straining. (a) Schematic drawing of the Cu grid for straining tests and SEM image of FIB-prepared foil. (b) TEM bright-field image of the thin foil before deformation. (c) Diffraction contrast STEM image after straining tests. Schematic drawing in the inset shows the slip planes of the dislocations. (d) TEM bright-field image showing highly curved line shape of glide dislocations and slip traces during deformation. (e) Diffraction contrast STEM image showing dislocation pile-ups in the sample after deformation.

thin foil, and followed by planar slip of dislocations. And, deformation twinning was not observed at all. The dislocation line shape is wavy and complicated during and even after deformation (Figure 4(c–e)).

In a thin foil TEM sample, dislocations intersect the top and bottom surfaces of the foil and bow out toward the gliding direction with forming a radius of curvature depending on the applied shear stress and strength of active pinning sites (Figure 5(a,b) and Supplementary Video 3,4). Then, they become more or less straight once the applied stress is released as a consequence of the dislocation line tension. We measured the shear stress acting on dislocations by fitting the line curvature of individual dislocations to a circle with the radius of R by using the equation, $\tau = \mu b/R$ [26], where μ is the shear modulus (80 GPa [27]) and b is the magnitude of the Burgers vector (0.255 nm). The inclination angle of the slip plane with respect to the image plane was calibrated through slip trace analysis. Figure 5(c,d) show the variations in the shear stress value on two representative dislocations and their position over time. The average shear stresses are 525 ± 65 MPa and 465 ± 62 MPa, respectively, where the error margin is the standard deviation of data points over time. The shear stress can be converted to normal stress of 850–1100 MPa by taking account of the local Schmid factors. The stress values follow size-dependent mechanical data in Figure 3(c), supporting that the observed dislocation glide motion represents the dominating deformation mechanism in HEA submicron pillars.

There are three possible contributions to this high shear stress required for dislocation glide. Firstly, surface oxide and/or FIB-damage layers restrict dislocation motion. Both ends of the dislocation lines are strongly attached to the surface and drag dislocation segments. Second, geometrical confinement by the film thickness shortens the dislocation line length and increases the required stress for their glide, referred to as thin foil effects [28]. Lastly, the inherent lattice friction stress contributes to the stress acting on dislocations.

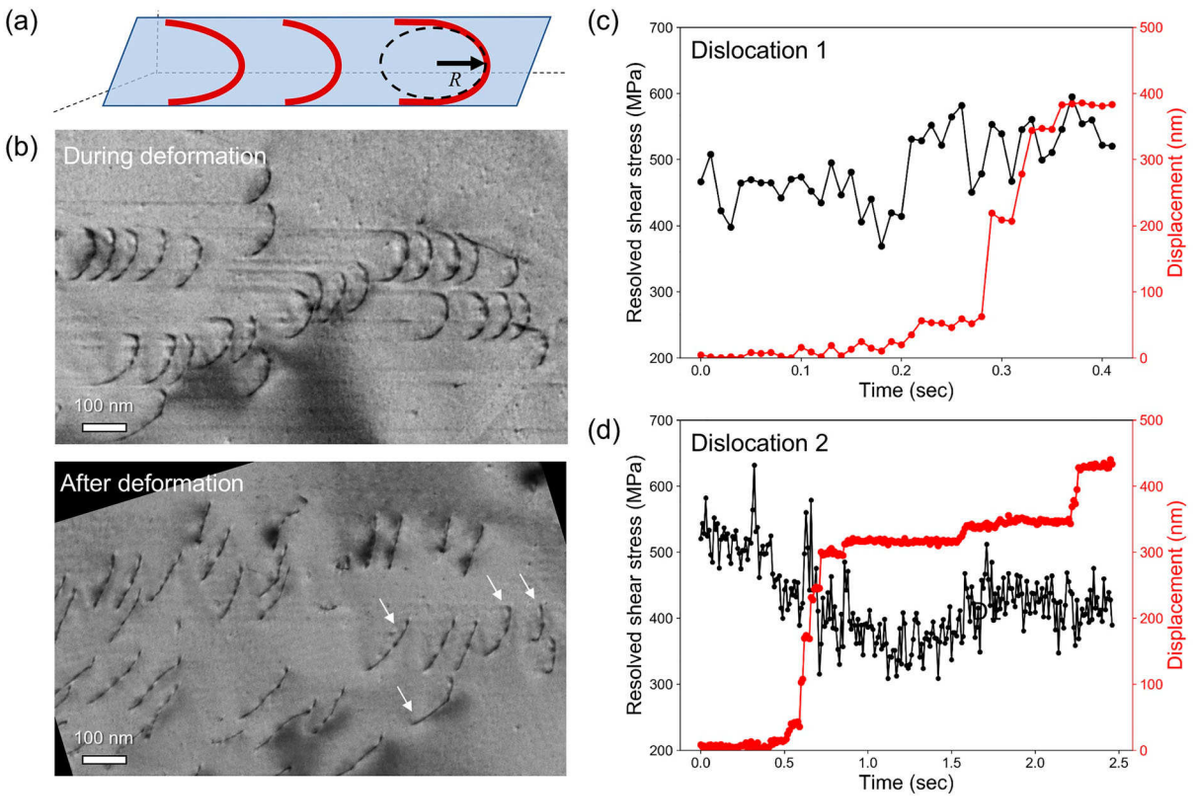

Figure 5. Evolution of the line curvature of dislocations during glide. (a) Schematic drawing of bowed dislocations gliding in a thin foil. (b) TEM images showing the array of dislocations during and after deformation. During glide, dislocations are bowed out in response to the local resolved shear stress but become more or less straight when the stress is released. Some of the dislocations (white arrows) are still curved even after the release of the external stress. (c, d) Threshold stresses for dislocation movement for two different dislocations as examples. The glide distances which show jerky motion with abrupt increase in displacements.

The combination of final milling at 5 keV Ga ion energy, followed by low energy Ar milling at 0.3 keV effectively reduces the FIB-damage layer thickness to less than 5 nm. All *in situ* TEM samples had a thickness of ~ 100 nm and hence the FIB-induced damage layer is less than 10% of the total specimen thickness. Furthermore, since the line curvature of dislocations was measured only in the middle section of the dislocations, which corresponds to the central part of the TEM foil, the effects of the surface damage layer on dislocation motion are considered to be small.

To compare the measured shear stress values with those of other FCC alloys, we applied the same analysis procedure to dislocations presented in literature for similar *in situ* TEM deformation experiments [29,30]. For instance, in the case of a high Mn steel, the shear stress was determined to be in the range of 170–250 MPa at room temperature [29] and 90–140 MPa for a 304 steel at 400 °C [30]. These values are significantly smaller than data obtained by us on the HEA. Note that the data determined from the literature references correspond to the upper bound of shear stress values since the exact inclination of the slip planes with respect to the observation direction was unknown.

Some of the dislocations (arrows in Figure 5(b)) are still curved even after the release of the external stress and the local shear stress measured from their curvature is 144.3 ± 56 MPa. High lattice friction stress and/or SRO might hinder dislocations from returning back to straight line shape. This value might be higher than in bulk due to surface pinning sites.

Another interesting feature in dislocation glide was that the glide motion was not continuous but shows jerky behavior (Supplementary Video 3,4). The displacement of dislocations shows step-wise abrupt increment (Figure 5(c)), which is also closely connected to the high lattice friction stress. Similarly, jerky flow of dislocations was also observed by *in situ* TEM deformation in nano-precipitation hardened and irradiated austenitic steels [29,30]. In a high Mn steel, dislocation motion was hindered by nanometer-sized κ-carbide precipitates [29] or in the case of an irradiated 304 steel by irradiation-induced defects [30]. However, as we discussed above, the surface-near FIB-damage effect is unlikely to dominate

the friction stress measurement. Also, we could not find any indication of precipitate formation by TEM diffraction, STEM-EDS and APT elemental mapping. Therefore, the severe lattice distortion introduced by multi principal elements or local chemical clustering (or SRO) could be responsible for hindering dislocation motion and leading to an increase in the lattice friction stress in HEA.

4. Conclusion

In summary, we have studied the dislocation plasticity in FeCoCrMnNi alloy in combination with atomic-scale chemical analysis and mechanical testing by *in situ* TEM deformation tests. The key conclusions are summarized as follows:

- The size exponent of our HEA submicron pillars is 0.53 ± 0.03 which is smaller compared to other FCC metals indicating higher lattice friction compared to typical FCC crystals.
- With electron diffraction, STEM-EDS and APT, we did not observe any chemical heterogeneity or ordered structures of sizes down to the resolution limits of 1 nm.
- Dislocation glide was in a jerky manner and their line shape is wavy with lots of pinning points.
- Even after unloading dislocations remain slightly curved revealing that frictional stresses of ~ 140 MPa.

Acknowledgments

This work was supported by Alexander von Humboldt Foundation; by SPP2006 CCA-HEA; and by the Creative Materials Discovery Program through the National Research Foundation of Korea (NRF) funded by the Ministry of Science and ICT (NRF-2015M3D1A1070672, NRF-2019M3D1A1078296), Bio-inspired Innovation Technology Development Project (NRF-2018M3C1B7021994) and Industrial Technology Innovation Program (10080654) of the Ministry of Trade, Industry & Energy (MOTIE, Korea).

Disclosure statement

No potential conflict of interest was reported by the author(s).

Funding

This work was supported by Alexander von Humboldt Foundation; by SPP2006 CCA-HEA; and by the Creative Materials Discovery Program through the National Research Foundation of Korea (NRF) funded by the Ministry of Science and ICT (NRF-2015M3D1A1070672, NRF-2019M3D1A1078296), Bio-inspired Innovation Technology Development Project (NRF-2018M3C1B7021994) and Industrial Technology Innovation Program (10080654) of the Ministry of Trade, Industry & Energy (MOTIE, Korea); Alexander von Humboldt-Stiftung; Korea Institute of Energy Technology Evaluation and Planning.

ORCID

Subin Lee http://orcid.org/0000-0002-4629-8004
María Jazmin Duarte http://orcid.org/0000-0001-7951-7640
Michael Feuerbacher http://orcid.org/0000-0003-2882-4960
Christoph Kirchlechner http://orcid.org/0000-0003-2418-9664
Sang Ho Oh http://orcid.org/0000-0001-5808-7821

References

[1] Gludovatz B, Hohenwarter A, Catoor D, et al. A fracture-resistant high-entropy alloy for cryogenic applications. Science (80-.). 2014;345:1153–1158.
[2] Tsai MH, Yeh JW. High-entropy alloys: a critical review. Mater Res Lett. 2014;2:107–123.
[3] Otto F, Dlouhý A, Somsen C, et al. The influences of temperature and microstructure on the tensile properties of a CoCrFeMnNi high-entropy alloy. Acta Mater. 2013;61:5743–5755.
[4] Cantor B, Chang ITH, Knight P, et al. Microstructural development in equiatomic multicomponent alloys. Mater Sci Eng A. 2004;375–377:213–218.
[5] Yeh JW, Chen SK, Lin SJ, et al. Nanostructured high-entropy alloys with multiple principal elements: novel alloy design concepts and outcomes. Adv Eng Mater. 2004;6:299–303.
[6] Laplanche G, Kostka A, Horst OM, et al. Microstructure evolution and critical stress for twinning in the CrMnFeCoNi high-entropy alloy. Acta Mater. 2016;118:152–163.
[7] Varvenne C, Luque A, Curtin WA. Theory of strengthening in fcc high entropy alloys. Acta Mater. 2016;118:164–176.
[8] Nöhring WG, Curtin WA. Correlation of microdistortions with misfit volumes in high entropy alloys. Scr Mater. 2019;168:119–123.
[9] Smith TM, Hooshmand MS, Esser BD, et al. Atomic-scale characterization and modeling of 60° dislocations in a high-entropy alloy. Acta Mater. 2016;110:352–363.
[10] Wang P, Wu Y, Liu J, et al. Impacts of atomic scale lattice distortion on dislocation activity in high-entropy alloys. Extrem Mech Lett. 2017;17:38–42.
[11] Zhang FX, Zhao S, Jin K, et al. Local structure and short-range order in a NiCoCr solid solution alloy. Phys Rev Lett. 2017;118:205501.
[12] Ding Q, Zhang Y, Chen X, et al. Tuning element distribution, structure and properties by composition in high-entropy alloys. Nature. 2019;574:223–227.
[13] Ding J, Yu Q, Asta M, et al. Tunable stacking fault energies by tailoring local chemical order in CrCoNi medium-entropy alloys. Proc Natl Acad Sci U S A. 2018;115:8919–8924.
[14] Liu J, Chen C, Xu Y, et al. Deformation twinning behaviors of the low stacking fault energy high-entropy alloy: an in-situ TEM study. Scr Mater. 2017;137:9–12.

[15] Zhang Z, Sheng H, Wang Z, et al. Dislocation mechanisms and 3D twin architectures generate exceptional strength-ductility-toughness combination in CrCoNi medium-entropy alloy. Nat Commun. 2017;8:14390.
[16] Moody MP, Stephenson LT, Ceguerra AV, et al. Quantitative binomial distribution analyses of nanoscale like-solute atom clustering and segregation in atom probe tomography data. Microsc Res Tech. 2008;71:542–550.
[17] Watanabe M, Ackland DW, Burrows A, et al. Improvements in the X-ray analytical capabilities of a scanning transmission electron microscope by spherical-aberration correction. Microsc Microanal. 2006;12:515–526.
[18] Raghavan R, Kirchlechner C, Jaya BN, et al. Mechanical size effects in a single crystalline equiatomic FeCrCoMnNi high entropy alloy. Scr Mater. 2017;129:52–55.
[19] Dou R, Derby B. A universal scaling law for the strength of metal micropillars and nanowires. Scr Mater. 2009;61:524–527.
[20] Choi WS, De Cooman BC, Sandlöbes S, et al. Size and orientation effects in partial dislocation-mediated deformation of twinning-induced plasticity steel micro-pillars. Acta Mater. 2015;98:391–404.
[21] Dimiduk DM, Uchic MD, Parthasarathy TA. Size-affected single-slip behavior of pure nickel microcrystals. Acta Mater. 2005;53:4065–4077.
[22] Volkert CA, Lilleodden ET. Size effects in the deformation of sub-micron Au columns. Philos Mag. 2006;86:5567–5579.
[23] Okamoto NL, Fujimoto S, Kambara Y, et al. Size effect, critical resolved shear stress, stacking fault energy, and solid solution strengthening in the CrMnFeCoNi high-entropy alloy. Sci Rep. 2016;6:35863.
[24] Reichardt A, Lupinacci A, Frazer D, et al. Nanoindentation and in situ microcompression in different dose regimes of proton beam irradiated 304 SS. J Nucl Mater. 2017;486:323–331.
[25] Mompiou F, Legros M. Plasticity mechanisms in submicron Al fiber investigated by in situ TEM. Adv Eng Mater. 2012;14:955–959.
[26] Hull D, Bacon DJ. Introduction to dislocations. Oxford: Butterworth-Heinemann; 2011.
[27] Haglund A, Koehler M, Catoor D, et al. Polycrystalline elastic moduli of a high-entropy alloy at cryogenic temperatures. Intermetallics. 2015;58:62–64.
[28] Arzt E. Size effects in materials due to microstructural and dimensional constraints: a comparative review. Acta Mater. 1998;46:5611–5626.
[29] Kim S-D, Park JY, Park S-J, et al. Direct observation of dislocation plasticity in high-Mn lightweight steel by in-situ TEM. Sci Rep. 2019;9:15171.
[30] Kacher J, Liu GS, Robertson IM. In situ and tomographic observations of defect free channel formation in ion irradiated stainless steels. Micron. 2012;43:1099–1107.